INORGANIC CHEMISTRY
FRONTIERS

RESEARCH ARTICLE

View Article Online
View Journal | View Issue

Cite this: *Inorg. Chem. Front.*, 2019, **6**, 1209

Graphene/graphene nanoribbon aerogels decorated with S-doped $MoSe_2$ nanosheets as an efficient electrocatalyst for hydrogen evolution†

Wei Fan,[a] Dong Wang,[a] Zhen Sun,[a] Xing Yi Ling *[b] and Tianxi Liu *[a]

Searching for an efficient and cost effective electrochemical catalyst is regarded as the key challenge for the hydrogen evolution reaction (HER). Both the active sites and electrical conductivity of the catalysts should be carefully engineered to improve their HER performance. In this work, S-doped $MoSe_2$-decorated graphene/graphene nanoribbon aerogel (S-$MoSe_2$@GGNR) hybrids have been fabricated as high-performance electrocatalysts for HER. The unique nanoribbon-interconnected-nanosheet structure of the graphene/graphene nanoribbon aerogel (GGNR) provides an open structure for fast ion diffusion and conductive channels for fast electron transport. GGNR as a substrate could prevent $MoSe_2$ nanosheets from agglomeration and fully expose the active sites of $MoSe_2$, while further S-doping can modify its electronic and crystalline structure, which can improve the activity of the catalytic sites. Consequently, the S-$MoSe_2$@GGNR hybrids exhibit outstanding electrochemical activity with a potential of −153 mV *vs.* reversible hydrogen electrode to achieve a current density of 10.0 mA cm^{-2} and a small Tafel slope of 46 mV per decade. The good performance of the S-$MoSe_2$@GGNR hybrids can be credited to synergistic effects between the unique hierarchical architecture of carbon aerogels and positive effect of S-doping, which makes them promising electrocatalysts for hydrogen production.

Received 15th January 2019,
Accepted 22nd March 2019

DOI: 10.1039/c9qi00064j

rsc.li/frontiers-inorganic

Introduction

Water electrolysis is one of the efficient approaches for the production of hydrogen through the hydrogen evolution reaction (HER), which is greatly dependent on the HER catalysts.[1–3] So far, the most active HER catalysts for water electrolysis are noble metals such as platinum, whose practical application is restricted by the extremely high cost and low elemental reserve. Hence, researchers were inspired to search for earth-abundant, cost-effective materials with both high HER activity and good catalytic stability. Various kinds of electrocatalysts were developed, including Pt alloy, non-noble metal and metal-free carbon materials.[4–7]

Among these candidates, layered transition metal dichalcogenides (TMDs), such as MoS_2, $MoSe_2$ and WS_2, have drawn much attention.[8–16] $MoSe_2$, one of the typical TMDs, has been reported with superior catalytic activity for HER due to the narrower bandgap and greater metallic nature than MoS_2.[17,18] However, bulk $MoSe_2$ exhibit poor HER performance due to the limited exposure of catalytic active sites. Active site engineering is one effective approach to improve their catalytic activity, emphasizing increasing exposed active sites and enhancing the intrinsic reactivity. First, designing layered metal dichalcogenides into nanostructures is the primary strategy to expose active sites.[19] Exfoliating bulk $MoSe_2$ into few-layered $MoSe_2$ nanosheets,[20,21] fabricating defect-rich $MoSe_2$,[22,23] and creating nanoporous structures[10,24] are explored for preferable catalytic performance. For example, Cui and coworkers reported vertically aligned few-layered $MoSe_2$ grown on Si nanowires, forming $MoSe_2$ thin films with ample exposed edges, resulting in improved HER performance.[25] Second, for enhancing the intrinsic reactivity of catalytic active materials, the representative way is heteroatom doping to tune their electronic structures.[26,27] For example, a Co-promoted S-edge showed reduced free energy of hydrogen adsorption, thus improving the activity of the edge sites of Co-doped MoS_2 nanomaterials.[28] Moreover, $MoS_{2(1-x)}Se_{2x}$ alloy nanoflakes exhibited improved HER activity compared to either MoS_2 or $MoSe_2$, which results from the modified d band electronic structure of molybdenum with incorporation of selenium and sulfur simultaneously.[29–36]

[a]*State Key Laboratory for Modification of Chemical Fibers and Polymer Materials, College of Materials Science and Engineering, Innovation Center for Textile Science and Technology, Donghua University, 2999 North Renmin Road, Shanghai 201620, P. R. China. E-mail: txliu@fudan.edu.cn, txliu@dhu.edu.cn*
[b]*Division of Chemistry and Biological Chemistry, School of Physical and Mathematical Sciences, Nanyang Technological University, 21 Nanyang Link, Singapore 637371, Singapore. E-mail: xyling@ntu.edu.sg*

†Electronic supplementary information (ESI) available: Experimental section and supplementary figures. See DOI: 10.1039/c9qi00064j

Another effective method to improve HER activity is electronic conductibility engineering.[37–40] Coupling $MoSe_2$ nanosheets with conductive carbon species can facilitate the catalytic activity by creating internal electron transport pathways between $MoSe_2$ and electrodes.[41–47] For example, Liu synthesized few-layered $MoSe_2$ nanosheets perpendicularly grown on conductive carbon nanotubes (CNTs), which facilitate the electron transfer inside the catalysts, thus resulting in enhanced HER performance.[48] Further study has shown that designing carbon nanomaterials into three-dimensional (3D) structures could not only facilitate electron transport but also shorten the ion transfer channels of catalysts, leading to superior HER activity.[49–55] However, the porous structure of carbon materials should be well designed to meet the desired electrocatalytic performance. Our previous work has shown that graphene/graphene nanoribbon (GGNR) aerogels with tunable 3D porous structure can optimize the electron transport and ion diffusion channels of the catalysts.[56] Although some studies have been reported to seek for a reasonable route for more superior $MoSe_2$-based electrocatalytic materials, the engineering of both conductivity and active sites for $MoSe_2$ nanosheets simultaneously still remains a great challenge.

In this study, with both active site and electronic conductibility engineering approaches in mind, sulfur-doped $MoSe_2$ decorated GGNR (S-$MoSe_2$@GGNR) hybrids have been designed and fabricated. Few-layered $MoSe_2$ nanosheets were first grown on GGNR aerogels, which were subsequently calcined with sulfur to obtain the S-$MoSe_2$@GGNR hybrid. The GGNR aerogels can facilitate catalytic activity by ensuring good electrical contact between $MoSe_2$ nanosheets and the electrodes. GGNR aerogels can also prevent $MoSe_2$ nanosheets from aggregating, which maximizes the number of exposed active sites. Moreover, S-doping can create more unsaturated S and Se edge sites and modify the d band electronic structure of molybdenum, which can further improve the electrocatalytic performance. Benefiting from both improved electrical conductivity and more active sites, the optimized S-$MoSe_2$@GGNR hybrid exhibits excellent HER performance, with a low onset potential and long-term stability in acid medium.

Experiment

Preparation of S-$MoSe_2$@GGNR hybrids

The graphene/graphene nanoribbon (GGNR) aerogel was prepared according to our previous work.[56] Typically, graphene oxide (GO, 4 mg mL^{-1}) and graphene oxide nanoribbon (GONR, 4 mg mL^{-1}) suspension were mixed in the proportion of 1 : 1, followed by freeze-drying and thermal treatment (900 °C for 2 h in N_2) to obtain GGNR aerogels (see details in ESI†).

$MoSe_2$@GGNR hybrids were fabricated *via* a solvothermal reaction, as schematically illustrated in Fig. 1. First, Na_2MoO_4 was added into 2 mg mL^{-1} Se solution in 10 mL $N_2H_4{\cdot}H_2O$ with the Mo : Se molar ratio of 1 : 2. 10 mL DMF was added to the above mixture along with sonication and then transferred to a 50 mL Teflon-lined autoclave. 10 mg GGNR aerogel was added into the autoclave, and the system was maintained at 180 °C for 12 h. S-$MoSe_2$@GGNR hybrids were further prepared by annealing the products in N_2 atmosphere at 450 °C for 2 h with the addition of S powder placed at the upstream side of the furnace. S-Doped $MoSe_2$@GGNR hybrids prepared with different amounts of S powder with weight ratio to $MoSe_2$@GGNR of 1 : 1, 1 : 2, and 1 : 4 were denoted as 1S-$MoSe_2$@GGNR, 2S-$MoSe_2$@GGNR and 4S-$MoSe_2$@GGNR, respectively. In addition, $MoSe_2$@GGNR-0.5 and $MoSe_2$@GGNR-2 hybrids with varied loading of $MoSe_2$ were also obtained with different amount of Se solution (5 and 20 mL), respectively. Pure $MoSe_2$ and S-$MoSe_2$ was also produced *via* the above method without GGNR aerogels.

Electrochemical characterization

Electrochemical measurements were performed in a three-electrode setup on an electrochemical workstation (CHI 660D,

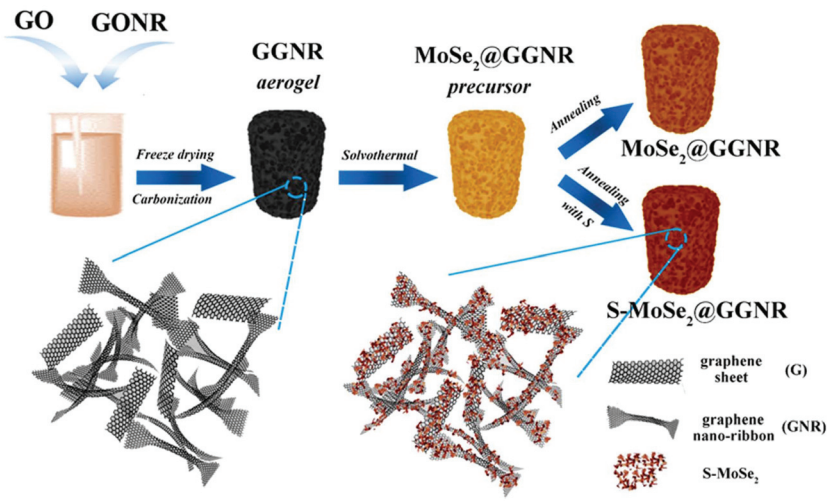

Fig. 1 Schematic illustration of the fabrication process of $MoSe_2$@GGNR and S-$MoSe_2$@GGNR hybrids.

Shanghai Chenhua Instrument Co., China), in which the catalyst-modified glassy carbon electrode (GCE) was used as the working electrode, the graphite rod as the counter electrode, and saturated calomel electrode (SCE) as the reference electrode, respectively. Typically, 4 mg of electrochemical catalyst were dispersed in a mixed solution of 1 mL water–ethanol and 20 μL of Nafion solution. After that, 5 μL of the slurry was loaded onto a glassy carbon electrode (3 mm diameter) with the mass loading of 0.28 mg cm^{-2} on each electrode. Linear sweep voltammetry (LSV) was conducted in 0.5 M N_2-purged H_2SO_4 solution with a scan rate of 2 mV s^{-1}. All the potentials reported in this work were calibrated to the reversible hydrogen electrode (RHE) according to the equation of $E_{RHE} = E_{SCE} + (0.241 + 0.059\ pH)$ V. The double-layer capacitance (C_{dl}) of the products was calculated from the cyclic voltammograms (CVs) in the region of 0.15–0.25 V *vs.* RHE. By plotting Δj at 0.2 V *vs.* RHE against the scan rate, the slope is twice that of C_{dl}. Electrochemical impedance spectroscopy (EIS) measurements were carried out in the frequency range between 100 kHz and 10 mHz with an amplitude of 5 mV.

Results and discussion

Morphology and structure of S-$MoSe_2$@GGNR

The morphology of S-$MoSe_2$@GGNR is shown in Fig. 2. The SEM image of the S-$MoSe_2$@GGNR aerogel at low magnification (Fig. 2a) shows a porous structure with ultrathin graphene sheets interconnected with each other. A close observation (Fig. 2b) shows that GNRs with the original ribbon-like morphology are distributed uniformly among the graphene sheets without aggregations, forming a nanoribbon-interconnected-nanosheet structure. The GNR-interconnected-graphene nanostructure can improve the electrical conductivity of the whole hybrid catalyst, thus facilitating the rapid transfer of electrons. Furthermore, planar graphene sheets and nanoribbons allow the intimate growth of highly dispersed and perpendicularly oriented $MoSe_2$ nanosheets. At high magnifications, it can be observed clearly that S-$MoSe_2$ nanosheets are evenly and perpendicularly distributed on the aerogel surface, both on the surface of GNRs (Fig. 2c) and graphene sheets (Fig. 2d). The TEM image of S-$MoSe_2$@GGNR also shows the uniform distribution of S-$MoSe_2$ nanosheets on a single graphene sheet (Fig. S1†). This uniformly and perpendicularly oriented nanosheet structure can increase the exposure of active edges, which is preferable for enhanced HER performance. In contrast, for pure $MoSe_2$ without the carbon aerogel template (Fig. S2†), $MoSe_2$ nanosheets seriously aggregate into a hydrangea-like morphology, thus hindering the exposure of the edge sites of $MoSe_2$. As indicated by the nitrogen adsorption/desorption isotherms shown in Fig. S3,† the specific surface area of S-$MoSe_2$@GGNR aerogels is 131 $m^2\ g^{-1}$, which is much larger than that of pure $MoSe_2$ nanosheets (18 $m^2\ g^{-1}$), highlighting the importance of the carbon aerogel template by constructing a homogeneous porous structure.

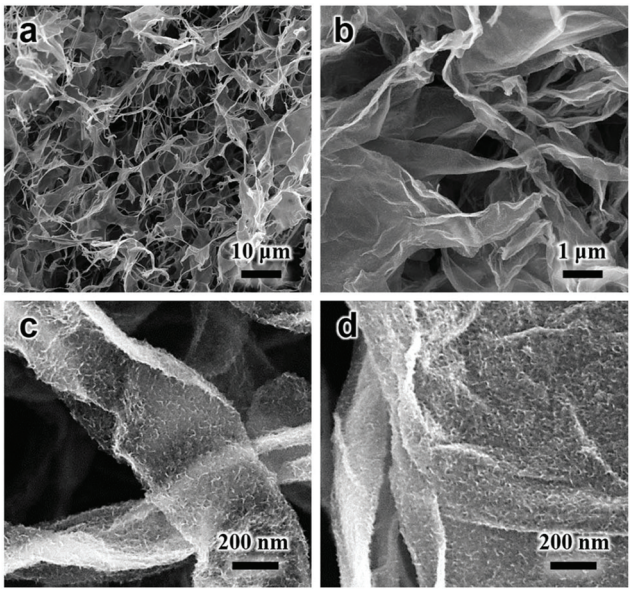

Fig. 2 SEM images of the 2S-$MoSe_2$@GGNR hybrid at (a) low and (b) high magnifications. (c) and (d) show $MoSe_2$ nanosheets growing uniformly on the GNR surface and graphene sheets, respectively.

The detailed microstructure of $MoSe_2$@GGNR and S-$MoSe_2$@GGNR hybrids was further observed using TEM (Fig. 3). The surface of the GGNR aerogels is covered with curved $MoSe_2$ nanosheets (Fig. 3a). The HRTEM image (Fig. 3b and c) further elucidates that the $MoSe_2$ nanosheets exhibit layered structures, with an interlayer spacing of about 0.65 nm, which is consistent with the (002) lattice of the annealed $MoSe_2$. The EDX mapping (Fig. 3d) of $MoSe_2$@GGNR hybrid reveals the uniform and homogeneous distribution of Mo, Se and C across the hybrid. For the S-$MoSe_2$@GGNR hybrid, it can be observed that a few-layered $MoSe_2$ nanosheets still adhered in an intact manner to the surface of GGNR from the TEM images in Fig. 3e, suggesting that the overall morphology would not be damaged through the S-doping process. However, the incorporation of S into $MoSe_2$ nanosheets in the 2S-$MoSe_2$@GGNR hybrid gives rise to more stacking faults and plane defects (Fig. 3e–g), resulting in the polycrystalline feature of the basal plane composed of distributed nanodomains. Different from the perfect crystal structure of the $MoSe_2$@GGNR hybrid (white box in Fig. 3c), the crystalline nanodomains (white box in Fig. 3g) and amorphous nanodomains (white circle in Fig. 3g) appear alternately in the basal plane of the 2S-$MoSe_2$@GGNR hybrid, resulting in the formation of additional unsaturated S and Se edge sites along the domain walls, which are possible active sites for HER catalysis. The EDX mapping of 2S-$MoSe_2$@GGNR hybrid presented in Fig. 3h indicates the homogeneous distribution of the S element throughout the hybrid.

The XRD patterns of $MoSe_2$@GGNR hybrids (Fig. 4a) reveal characteristic peaks at $2\theta = 13.6°$, 26.2°, 31.8°, 37.6° and 56.1°, corresponding to the diffraction planes of (002), (004), (100), (103) and (110) for $MoSe_2$ (JCPDS 29-0914), respectively. The broad peak centered at $2\theta = 26°$ can be assigned to amorphous

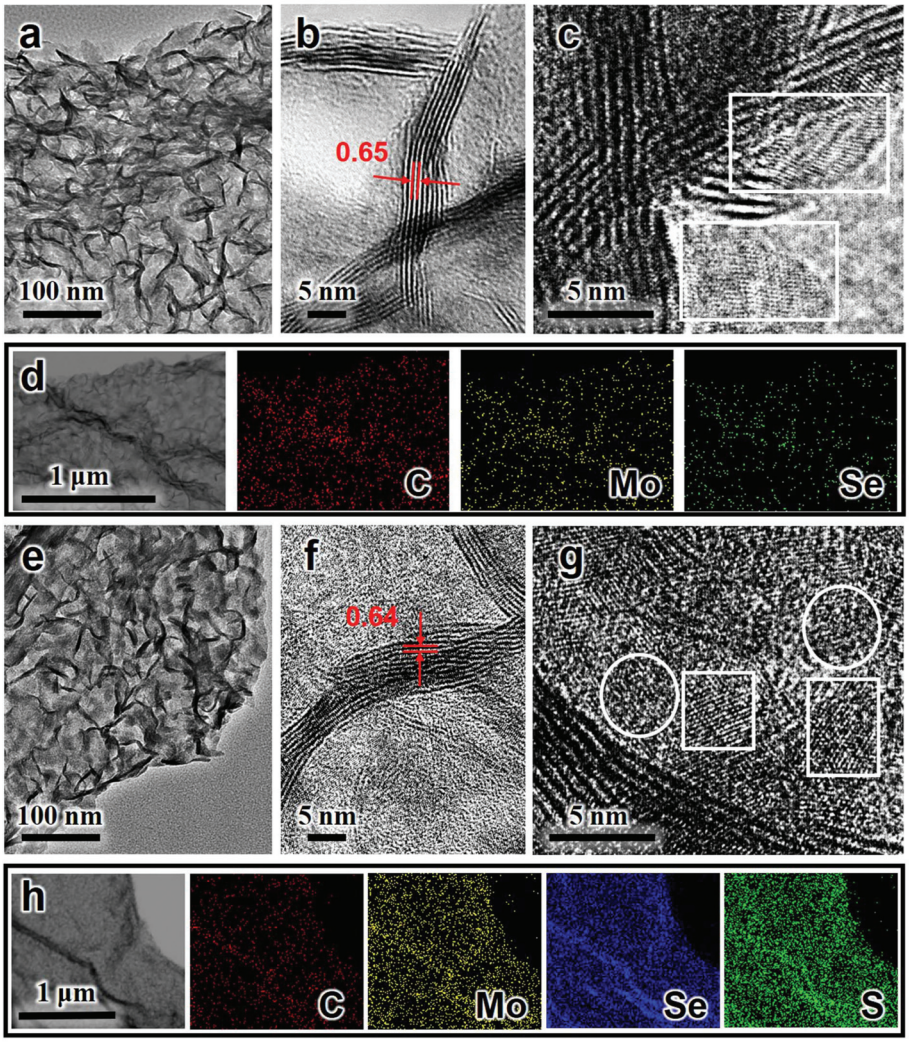

Fig. 3 (a–c) TEM images of the $MoSe_2$@GGNR hybrid at different magnifications. (d) Corresponding elemental mapping of the C, Mo and Se elements, respectively. (e–g) TEM images of the 2S-$MoSe_2$@GGNR hybrid at different magnifications. (h) Corresponding elemental mapping of the C, Mo, Se and S elements, respectively.

carbon, which is in accordance with the diffraction peak of GGNR, suggesting that $MoSe_2$ nanosheets and GGNR are successfully composited in the $MoSe_2$@GGNR hybrid. For the S-doped samples, with increasing S content, the (100) and (110) peaks gradually shift to higher 2θ angles as illustrated by dotted line in Fig. 4a. This agrees with the modification in the lattice parameter (high-magnification TEM images in Fig. 3) through the replacement of selenium atoms with smaller sulfur atoms, indicating their mixing at the atomic level. Fig. 4b presents the Raman spectra of S-$MoSe_2$@GGNR hybrids. All the spectra show the typical D band (~1354 cm^{-1}) and G band (~1588 cm^{-1}) of carbon materials, confirming the existence of the GGNR aerogel. The $MoSe_2$@GGNR hybrid shows a peak located at 238 cm^{-1}, corresponding to the typical $A_{1g\ (Mo-Se)}$ mode of $MoSe_2$. With the introduction of S, the peak intensity of the $A_{1g\ (Mo-Se)}$ mode weakened and two peaks located at 384 cm^{-1} and 402 cm^{-1} appeared, contributing to $E^1_{2g\ (Mo-S)}$ and $A_{1g\ (Mo-S)}$ modes, indicating the substitution of Se by S atoms. With the increase of S, the E^1_{2g} modes (~283 cm^{-1}) related to Mo–Se shift to lower wavenumber in the S-$MoSe_2$@GGNR hybrids, indicating the decreased vibration frequency of the Mo–Se modes through the interaction between sulfur and selenium atoms.

The XPS survey spectra in Fig. 4c indicate the presence of Mo, Se, C, and O elements in the $MoSe_2$@GGNR hybrid, while the S element can also be found in S-$MoSe_2$@GGNR hybrids, which is in agreement with the EDX results (Fig. 3d and h). The Se/S molar ratios of 1S-$MoSe_2$@GGNR, 2S-$MoSe_2$@GGNR and 4S-$MoSe_2$@GGNR are determined to be 1.35 : 0.65, 1.06 : 0.94 and 0.89 : 1 : 21, respectively. The Mo 3d spectrum (Fig. 4d) of the $MoSe_2$@GGNR hybrids exhibits two peaks at 228.7 and 232.1 eV assigned to Mo $3d_{5/2}$ and Mo $3d_{3/2}$ orbitals, respectively, confirming the formation of Mo^{4+}. The introduction of S causes a gradual shift of Mo $3d_{5/2}$ and Mo $3d_{3/2}$ to higher binding energy to 229.4 and 232.6 eV in 4S-$MoSe_2$@GGNR, respectively, suggesting that varying S contents in $MoSe_2$@GGNR

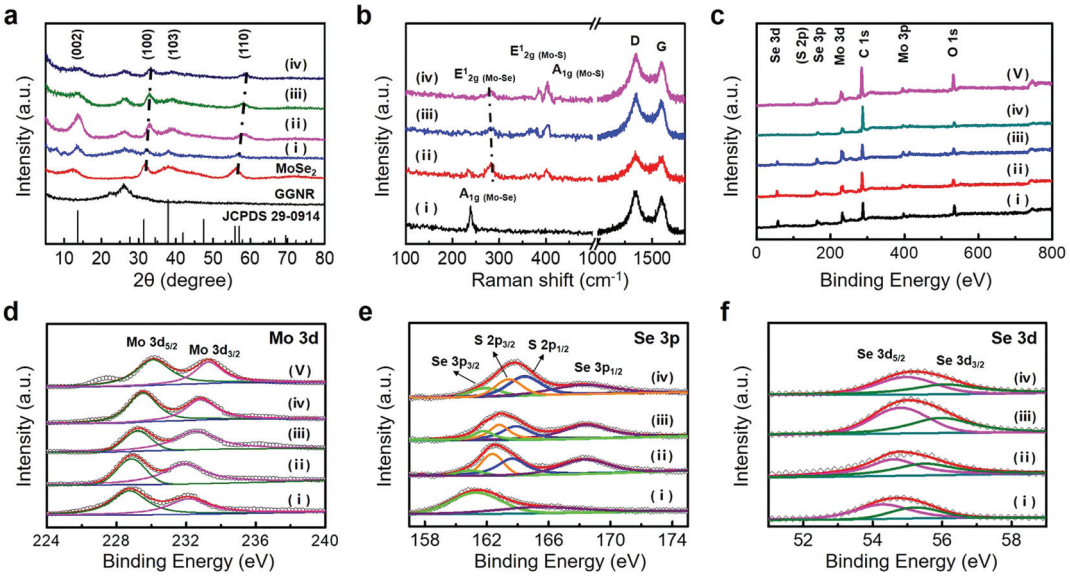

Fig. 4 (a) XRD patterns, (b) Raman spectra, and (c) XPS spectra for the hybrids. (d–f) High-resolution XPS spectra of Mo 3d, Se 3p and Se 3d, respectively. (i) $MoSe_2$@GGNR hybrid, (ii) 1S-$MoSe_2$@GGNR hybrid, (iii) 2S-$MoSe_2$@GGNR hybrid, (iv) 4S-$MoSe_2$@GGNR hybrid, and (v) MoS_2@GGNR hybrid.

hybrids would modify the d band electronic structure of molybdenum, which may lead to significant change in catalytic activity since d electrons in transition metals bond with adsorbates. Furthermore, a slight shift of Se 3p (Fig. 4e) and Se 3d (Fig. 4f) can be observed with increasing S amount. And the peaks located at ~162.4 eV and ~163.6 eV corresponding to S $2p_{3/2}$ and S $2p_{1/2}$ orbits of divalent sulfide ions (S^{2-}) rise continuously, implying the substitution of Se by S atoms.

HER electrocatalytic activity of S-$MoSe_2$@GGNR

The HER activities were investigated in 0.5 M H_2SO_4 solution at a scan rate of 2 mV s^{-1}. Fig. 5a shows the LSV curves for Pt/C, MoS_2, $MoSe_2$, $MoSe_2$@GGNR and the S-$MoSe_2$@GGNR hybrid. The Pt catalyst exhibits superb HER activity, with a near-zero overpotential and a large current density. Despite the highlighted theoretical catalytic activity of pure MoS_2 and

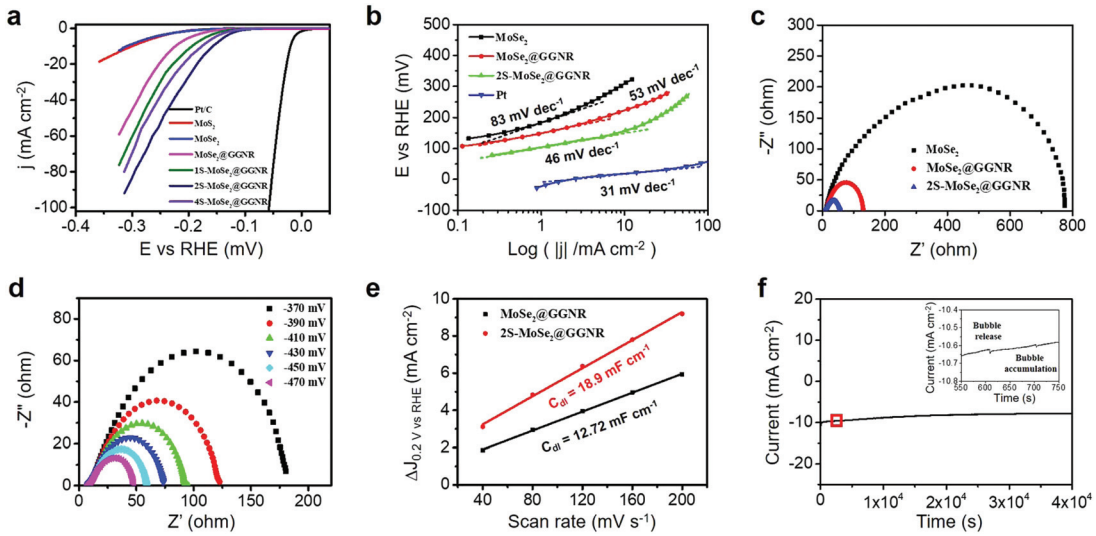

Fig. 5 (a) LSV polarization curves for Pt/C, MoS_2, $MoSe_2$, $MoSe_2$@GGNR hybrids, and S-$MoSe_2$@GGNR hybrids. (b) The corresponding Tafel plots. (c) Electrochemical impedance spectra of $MoSe_2$, $MoSe_2$@GGNR hybrids and 2S-$MoSe_2$@GGNR hybrids. (d) EIS of the 2S-$MoSe_2$@GGNR hybrid at various overpotentials. (e) Plots showing the extraction of the double layer capacitance (C_{dl}) for the $MoSe_2$@GGNR hybrids and 2S-$MoSe_2$@GGNR hybrids at 0.2 V. (f) Time dependence of the current density for the 2S-$MoSe_2$@GGNR hybrid modified GCE recorded at −0.16 V *versus* RHE in 0.5 M H_2SO_4 solution.

$MoSe_2$, the current density is much lower compared with those of the $MoSe_2$@GGNR hybrid, which can be ascribed to the aggregation of pure nanosheets with hindered active edges and poor electroconductivity (Fig. S2†). The better HER catalytic activity of the $MoSe_2$@GGNR hybrid highlights the important role of 3D carbon substrates that provide improved conductivity and exposed HER active sites. The catalytic performance of the $MoSe_2$@GGNR hybrids with different $MoSe_2$ loading are further investigated (Fig. S4†). The $MoSe_2$@GGNR hybrid with proper $MoSe_2$ loading shows the optimized HER performance, with the onset overpotential (η) of 90 mV and current density (j) of 10 mA cm^{-2} at η = 220 mV, which outperforms those of the other two samples. Notably, the S-$MoSe_2$@GGNR hybrid even exhibits preferable performance than the $MoSe_2$@GGNR hybrid. As shown in Fig. 5a, among all the S-doped $MoSe_2$@GGNR hybrids, 2S-$MoSe_2$@GGNR exhibits the best HER activity with an onset potential of 70 mV. Furthermore, the 2S-$MoSe_2$@GGNR hybrid shows a current density of 10.0 mA cm^{-2} at a low overpotential of 153 mV, compared with 195 mV required for 1S-$MoSe_2$@GGNR and 175 mV for the 4S-$MoSe_2$@GGNR hybrid. The HER activity is better than most MoS_2 or $MoSe_2$-based electrocatalysts as listed in Table 1. The enhanced HER performance of S-$MoSe_2$@GGNR hybrid with S-doping can be attributed to the following factors. First, S-doping would give rise to more crystal distortion and unsaturated S and Se edge sites (as shown in the TEM image in Fig. 3g), leading to increased defective sites and exposed active sites, which is beneficial for the improvement of resultant catalytic performance. Second, the modification of the d band electronic structure of $MoSe_2$ with appropriate S-doping (as shown in XPS spectra in Fig. 4d) can adjust the hydrogen adsorption energy and achieve ΔG_H close to thermoneutral, exerting a positive effect on the HER activity.

The Tafel plots are shown in Fig. 5b, which have originated from their corresponding LSV curves with the Tafel equation $\eta = b\log(j) + a$ (where η is the overpotential, b is the Tafel slope, and j is the current density). It should be noted that the 2S-$MoSe_2$@GGNR hybrid shows a lower Tafel slope of 46 mV dec^{-1}, suggesting that the fast HER reaction occurs through a Volmer–Heyrovsky mechanism with fast discharge reaction followed by a rate-limiting recombination step.[57,58] Nyquist plots (Fig. 5c) of the $MoSe_2$@GGNR hybrid show a much smaller charge transfer resistance (R_{ct}) of 120 Ω in comparison with that of $MoSe_2$ (762 Ω), reflecting faster electrode kinetics and lower transfer resistance due to the presence of a carbon aerogel in $MoSe_2$@GGNR. Besides, the R_{ct} of the 2S-$MoSe_2$@GGNR hybrid is even smaller (45 Ω), fully reflecting the preferable electron transfer from the appropriate S-doping. EIS responses of the 2S-$MoSe_2$@GGNR hybrid at various overpotentials (Fig. 5d) reveal that R_{ct} decreases with the increase of overpotential, indicating more rapid electron transfer and more efficient hydrogen generation under increased overpotentials. The electrochemical double layer capacitance (C_{dl}) was also measured to estimate the effective surface area of the solid–liquid interface for $MoSe_2$@GGNR and 2S-$MoSe_2$@GGNR (Fig. 5e and Fig. S5†). The 2S-$MoSe_2$@GGNR hybrid exhibits a higher C_{dl} of 18.9 mF cm^{-2} compared with that of $MoSe_2$@GGNR (C_{dl} = 12.7 mF cm^{-2}), indicating a larger exposed active area caused by the heteroatoms distorting the crystalline structure of $MoSe_2$.

Continuous HER activities at a constant overpotential were conducted to investigate the durability of 2S-$MoSe_2$@GGNR. As demonstrated in Fig. 5f, the current density displays only a slight fluctuation after long-term cycling of more than 10 h, revealing the good stability of the 2S-$MoSe_2$@GGNR catalyst. The inset in Fig. 5f further indicates the alternate bubble accumulation and release processes of hydrogen, indicating the rapid depletion of H^+ in the electrolyte. The faradaic efficiency of 2S-$MoSe_2$@GGNR is also determined. Potentiostatic electrolysis of 2S-$MoSe_2$@GGNR was performed and maintained 3600 s at an overpotential of 160 mV in 0.5 M

Table 1 Comparison of HER performance of MoS_2 or $MoSe_2$-based catalysts in 0.5 M H_2SO_4

Electrode materials	Onset potential (mV)	Tafel slope (mV dec^{-1})	η at 10.0 mA cm^{-2} (mV)	Ref.
1T@2H-$MoSe_2$/Ti	120	68	—	13
MoS_2–$MoSe_2$ heterostructures	—	46	175	18
Ultrathin S-doped $MoSe_2$ nanosheets	90	58	—	27
$MoS_{2(1-x)}Se_{2x}$ alloy nanoflakes	80–100	46	164	29
Monolayered $MoS_{2(1-x)}Se_{2x}$	—	119	273	31
$MoS_{2(1-x)}Se_{2x}$ nanotubes	101	55	219	35
MoS_2/graphitic nanocarbon hybrid	—	47	195	40
$MoSe_2$/carbon fiber cloth	70	69	182	45
1T-2H $MoSe_2$/graphene shell/core nanoflake	45	49	98	46
$MoSe_2$/graphene	50	61	159	47
Carbon nanotube@$MoSe_2$	70	58	178	48
MoS_2/carbon aerogel	140	59	200	49
MoS_2/mesoporous graphene	100	42	—	51
MoS_2/N-doped graphene aerogel	236	230	261	54
MoSSe@reduced graphene oxide	—	51	153	57
MoS_2 supported on MOF-derived carbon	35	53	200	59
$MoS_{2(1-x)}Se_{2x}$/carbon nanofibers	54	124	150	60
$MoSe_2$@GGNR	90	53	220	This work
2S-$MoSe_2$@GGNR	70	46	153	This work

H_2SO_4, and the corresponding amount of generated H_2 was measured using gas chromatography. As shown in Fig. S6,† the agreement of the amount of experimentally quantified hydrogen with theoretically calculated hydrogen (assuming 100% faradaic efficiency) suggests that the faradaic efficiency is close to 100%.

Conclusions

In summary, S-doped $MoSe_2$ nanosheet-decorated GGNR aerogel hybrids have been synthesized as efficient electrocatalysts for HER. The GGNR aerogel with a 3D interconnected open structure can facilitate the rapid transfer of electrons and fast ion diffusion, while the introduction of S modifies the electronic structure and crystalline structure of $MoSe_2$, further enhancing the catalytic performance of the hybrid. As a result, with both improved electrical conductivity and active sites, the optimal S-$MoSe_2$@GGNR hybrid exhibits excellent HER activity with a relatively low onset potential of −70 mV, and a small Tafel slope of 46 mV per decade. Therefore, this study provides an alternative material in exploiting the Pt-free HER catalyst with high performance.

Conflicts of interest

There are no conflicts to declare.

Acknowledgements

The authors are grateful for the financial support from the National Natural Science Foundation of China (21704014, 51433001, and 21674019), Science and Technology Commission of Shanghai Municipality (16520722100), the Fundamental Research Funds for the Central Universities (2232017D-06), Shanghai Municipal Education Commission (17CG33), Shanghai Sailing Program (17YF1400200), and Program of Shanghai Academic Research Leader (17XD1400100).

Notes and references

1 Y. M. Shi and B. Zhang, *Chem. Soc. Rev.*, 2016, **45**, 1529–1541.
2 D. P. Halter, F. W. Heinemann, J. Bachmann and K. Meyer, *Nature*, 2016, **530**, 317.
3 S. Wang, D. Zhang, B. Li, C. Zhang, Z. G. Du, H. M. Yin, X. F. Bi and S. B. Yang, *Adv. Energy Mater.*, 2018, **8**, 1801345.
4 J. Wang, F. Xu, H. Y. Jin, Y. Q. Chen and Y. Wang, *Adv. Mater.*, 2017, **29**, 1605838.
5 J. Kibsgaard and T. F. Jaramillo, *Angew. Chem., Int. Ed.*, 2014, **53**, 14433–14437.
6 Y. Yoo, Z. P. Degregorio and J. E. Johns, *J. Am. Chem. Soc.*, 2015, **137**, 14281–14287.
7 H. Y. Lu, W. Fan, Y. P. Huang and T. X. Liu, *Nano Res.*, 2018, **11**, 1274–1284.
8 Z. Wu, B. Fang, Z. Wang, C. Wang, Z. Liu, F. Liu, W. Wang, A. Alfantazi, D. Wang and D. P. Wilkinson, *ACS Catal.*, 2013, **3**, 2101–2107.
9 J. Lin, Z. Peng, G. Wang, D. Zakhidov, E. Larios, M. J. Yacaman and J. M. Tour, *Adv. Energy Mater.*, 2014, **4**, 130187510.
10 Y. Yang, H. Fei, G. Ruan, C. Xiang and J. M. Tour, *Adv. Mater.*, 2014, **26**, 8163–8168.
11 D. Z. Wang, Z. P. Wang, C. L. Wang, P. Zhou, Z. Z. Wu and Z. H. Liu, *Electrochem. Commun.*, 2013, **34**, 219–222.
12 X. Q. Wang, Y. F. Chen, B. J. Zheng, F. Qi, J. R. He, P. J. Li and W. L. Zhang, *Electrochim. Acta*, 2016, **222**, 1293–1299.
13 J. Zhang, Y. Chen, M. Liu, K. Du, Y. Zhou, Y. Li, Z. Wang and J. Zhang, *Nano Res.*, 2018, **11**, 4587–4598.
14 Y. Yan, B. Y. Xia, Z. C. Xu and X. Wang, *ACS Catal.*, 2014, **4**, 1693–1705.
15 J. Yang, K. Wang, J. X. Zhu, C. Zhang and T. X. Liu, *ACS Appl. Mater. Interfaces*, 2016, **8**, 31702–31708.
16 X. B. Zhu, L. L. Mo, Y. Wu, F. L. Lai, X. M. Han, X. Y. Ling, T. X. Liu and Y. E. Miao, *Compos. Commun.*, 2018, **9**, 86–91.
17 C. Tsai, K. Chan, F. Abild-Pedersen and J. K. Norskov, *Phys. Chem. Chem. Phys.*, 2014, **16**, 13156–13164.
18 J. Yang, J. X. Zhu, J. S. Xu, C. Zhang and T. X. Liu, *ACS Appl. Mater. Interfaces*, 2017, **9**, 44550–44559.
19 H. T. Wang, Z. Y. Lu, D. S. Kong, J. Sun, T. M. Hymel and Y. Cui, *ACS Nano*, 2014, **8**, 4940–4947.
20 J. Kibsgaard, Z. Chen, B. N. Reinecke and T. F. Jaramillo, *Nat. Mater.*, 2012, **11**, 963–969.
21 M. A. Lukowski, A. S. Daniel, F. Meng, A. Forticaux, L. Li and S. Jin, *J. Am. Chem. Soc.*, 2013, **135**, 10274–10277.
22 J. F. Xie, J. J. Zhang, S. Li, F. B. Grote, X. D. Zhang, H. Zhang, R. X. Wang, Y. Lei, B. C. Pan and Y. Xie, *J. Am. Chem. Soc.*, 2013, **135**, 17881–17888.
23 J. F. Xie, H. Qu, J. Xin, X. Zhang, G. Cui, X. D. Zhang, J. Bao, B. Tang and Y. Xie, *Nano Res.*, 2017, **10**, 1178–1188.
24 D. Y. Chung, S. Park, Y. Chung, S. Yu, D. Lim, N. Jung, H. C. Ham, H. Park, Y. Piao, S. J. Yoo and Y. Sung, *Nanoscale*, 2014, **6**, 2131–2136.
25 H. Wang, D. Kong, P. Johanes, J. J. Cha, G. Zheng, K. Yan, N. Liu and Y. Cui, *Nano Lett.*, 2013, **13**, 3426–3433.
26 D. Y. Wang, M. Gong, H. L. Chou, C. Pan, H. A. Chen, Y. P. Wu, M. C. Lin, M. Y. Guan, J. Yang, C. Chen, Y. Wang, B. J. Hwang, C. C. Chen and H. J. Dai, *J. Am. Chem. Soc.*, 2015, **137**, 1587–1592.
27 C. Xu, S. J. Peng, C. L. Tan, H. X. Ang, H. T. Tan, H. Zhang and Q. Y. Yan, *J. Mater. Chem. A*, 2014, **2**, 5597–5601.
28 Q. Z. Xiong, X. Zhang, H. J. Wang, G. Q. Liu, G. Z. Wang, H. M. Zhang and H. I. Zhao, *Chem. Commun.*, 2018, **54**, 3859–3862.
29 Q. F. Gong, L. Cheng, C. H. Liu, M. Zhang, Q. L. Feng, H. L. Ye, M. Zeng, L. M. Xie, Z. Liu and Y. G. Li, *ACS Catal.*, 2015, **5**, 2213–2219.

30 V. Kiran, D. Mukherjee, R. N. Jenjeti and S. Sampath, *Nanoscale*, 2014, **6**, 12856–12863.
31 L. Yang, Q. Fu, W. H. Wang, J. Huang, J. L. Huang, J. Y. Zhang and B. Xiang, *Nanoscale*, 2015, **7**, 10490–10497.
32 J. Zhang, W. Kang, M. Jiang, Y. You, Y. Cao, T. Ng, D. Y. W. Yu, C. Lee and J. Xu, *Nanoscale*, 2017, **9**, 1484–1490.
33 X. Zhou, J. Jiang, T. Ding, J. Zhang, B. Pan, J. Zuo and Q. Yang, *Nanoscale*, 2014, **6**, 11046–11051.
34 V. Kiran, D. Mukherjee, R. N. Jenjeti and S. Sampath, *Nanoscale*, 2014, **6**, 12856–12863.
35 J. Zhang, M. Wu, Z. Shi, M. Jiang, W. Jian, Z. Xiao, J. Li, C. Lee and J. Xu, *Small*, 2016, **12**, 4379–4385.
36 F. Ersan, G. Gökoğlu and E. Aktürk, *J. Phys. Chem. C*, 2015, **119**, 28648–28653.
37 H. H. Gu, Y. P. Huang, L. Z. Zuo, W. Fan and T. X. Liu, *Inorg. Chem. Front.*, 2016, **3**, 1280–1288.
38 Y. G. Li, H. L. Wang, L. M. Xie, Y. Y. Liang, G. S. Hong and H. J. Dai, *J. Am. Chem. Soc.*, 2011, **133**, 7296–7299.
39 A. P. Murthy, J. Madhavan and K. Murugan, *J. Power Sources*, 2018, **398**, 9–26.
40 W. Ma, H. R. Li, S. Y. Jiang, G. H. Han, J. Gao, X. M. Yu, H. L. Lian, W. F. Tu, Y. Han and R. Z. Ma, *ACS Sustainable Chem. Eng.*, 2018, **6**, 14441–14449.
41 A. P. Liu, L. Zhao, J. M. Zhang, L. X. Lin and H. P. Wu, *ACS Appl. Mater. Interfaces*, 2016, **8**, 25210–25218.
42 C. Zhen, B. Zhang, Y. Zhou, Y. Du and P. Xu, *Inorg. Chem. Front.*, 2018, **5**, 1386–1390.
43 S. Chen, J. Duan, Y. Tang, B. Jin and S. Z. Qiao, *Nano Energy*, 2015, **11**, 11–18.
44 W. Sun, P. Li, X. Liu, J. Shi, H. Sun, Z. Tao, F. Li and J. Chen, *Nano Res.*, 2017, **10**, 2210–2222.
45 B. Qu, X. B. Yu, Y. J. Chen, C. L. Zhu, C. Y. Li, Z. X. Yin and X. T. Zhang, *ACS Appl. Mater. Interfaces*, 2015, **7**, 14170–14175.
46 S. J. Deng, Y. Zhong, Y. X. Zeng, Y. D. Wang, Z. J. Yao, F. Yang, S. W. Lin, X. L. Wang, X. H. Lu, X. H. Xia and J. P. Tu, *Adv. Mater.*, 2017, **29**, 1700748.
47 S. Mao, Z. Wen, S. Ci, X. Guo, K. K. Ostrikov and J. Chen, *Small*, 2015, **11**, 414–419.
48 Y. P. Huang, H. Y. Lu, H. H. Gu, J. Fu, S. Y. Mo, C. Wei, Y. E. Miao and T. X. Liu, *Nanoscale*, 2015, **7**, 18595–18602.
49 Y. F. Zhang, L. Z. Zuo, Y. P. Huang, L. S. Zhang, F. L. Lai, W. Fan and T. X. Liu, *ACS Sustainable Chem. Eng.*, 2015, **3**, 3140–3148.
50 Y. Wang, D. Kong, W. Shi, B. Liu, G. J. Sim, Q. Ge and H. Y. Yang, *Adv. Energy Mater.*, 2016, **6**, 160105721.
51 L. Liao, J. Zhu, X. Bian, L. Zhu, M. D. Scanlon, H. H. Girault and B. Liu, *Adv. Funct. Mater.*, 2013, **23**, 5326–5333.
52 Y. Zhao, X. Xie, J. Zhang, H. Liu, H. Ahn, K. N. Sun and G. X. Wang, *Chem. – Eur. J.*, 2015, **21**, 15908.
53 S. K. Park, D. Y. Chung, D. J. Ko, Y. E. Sung and Y. Z. Piao, *J. Mater. Chem. A*, 2016, **4**, 12720–12725.
54 Y. Hou, B. Zhang, Z. H. Wen, S. M. Cui, X. R. Guo, Z. He and J. H. Chen, *J. Mater. Chem. A*, 2014, **2**, 13795–13800.
55 X. M. Liang and Q. F. Cheng, *Compos. Commun.*, 2018, **10**, 122–128.
56 Z. Sun, W. Fan and T. X. Liu, *Electrochim. Acta*, 2017, **250**, 91–98.
57 B. Konkena, J. Masa, W. Xia, M. Muhler and W. Schuhmann, *Nano Energy*, 2016, **29**, 46–53.
58 Y. Huang, R. J. Nielsen and W. A. Goddard, *J. Am. Chem. Soc.*, 2018, **140**, 16773–16782.
59 J. H. Feng, H. Zhou, J. P. Wang, T. Bian, J. X. Shao and A. H. Yuan, *Int. J. Hydrogen Energy*, 2018, **43**, 20538–20545.
60 H. Yang, T. Zhang, H. Zhu, M. Zhang, W. W. Wu and M. L. Du, *Int. J. Hydrogen Energy*, 2017, **42**, 1912–1918.